The Imbricated Foreshock and Aftershock Activities of the Balsorano (Italy) M_w 4.4 Normal Fault Earthquake and Implications for Earthquake Initiation

Hugo Sánchez-Reyes*[1], David Essing[1], Eric Beaucé[2], and Piero Poli[1]

Abstract

Foreshocks in the form of microseismicity are among the most powerful tools to study the physical processes that occur before main earthquakes. However, their detection and precise characterization is still sparse, especially for small-to-moderate-size earthquakes ($M_w < 6$). We present here a detailed foreshock analysis for the 7 November 2019, Balsorano, Italy, normal fault earthquake (M_w 4.4). To improve the detection of the microseismicity before and after the mainshock, we use six three-component broadband receivers at distances of less than 75 km from the targeted seismicity, through template matching. To improve the understanding of the physical mechanism(s) behind the earthquake initiation process, as well as other accompanying phenomena, we also detail the spatiotemporal evolution of the sequence associated with this medium-sized earthquake, using waveform clustering and hypocenter relocation. Clear differences between foreshocks and aftershocks are revealed by this analysis. Moreover, five distinct spatiotemporal patterns associated with the different seismic activities are revealed. The observed spatiotemporal behavior shown by the foreshocks highlights a complex initiation process, which apparently starts on an adjacent unmapped antithetic fault. Finally, the aftershock activity comprises four different clusters with distinct spatiotemporal patterns, which suggests that the different clusters in this sequence have distinct triggering mechanisms.

Cite this article as Sánchez-Reyes, H., D. Essing, E. Beaucé, and P. Poli (2021). The Imbricated Foreshock and Aftershock Activities of the Balsorano (Italy) M_w 4.4 Normal Fault Earthquake and Implications for Earthquake Initiation, *Seismol. Res. Lett.* **92**, 1926–1936, doi: 10.1785/0220200253.

Supplemental Material

Introduction

The detection of signals that can inform us about a forthcoming earthquake is fundamental to build physical models that mimic the processes behind the triggering and nucleation of earthquakes. These physical models are important because they provide us the basis to characterize earthquakes. Therefore, the study and analysis of precursory signals are of great importance. Over the last 25 yr, numerous studies have reported a wide range of observations that appear to be connected with the physics that precedes large seismic events (e.g., Rikitake, 1975; Jones and Molnar, 1979; Jones, 1985; Abercrombie and Mori, 1996; Dodge *et al.*, 1996; Molchanov *et al.*, 1998; Reasenberg, 1999; Eftaxias *et al.*, 2000; Virk and Walia, 2001; Felzer *et al.*, 2004; Singh *et al.*, 2010; Ruiz *et al.*, 2014, 2017; Ellsworth and Bulut, 2018; De Santis *et al.*, 2019; Yoon *et al.*, 2019). Among these, some of the most compelling are the ones based on seismological characterization of foreshock sequences, as well as other seismological observations and their relationships with mainshocks (e.g., Jones, 1985; Abercrombie and Mori, 1996; Dodge *et al.*, 1996; Reasenberg, 1999; Felzer *et al.*, 2004; Bouchon *et al.*, 2011; Ruiz *et al.*, 2014, 2017; Ellsworth and Bulut, 2018; Yoon *et al.*, 2019). Foreshocks are thus one of the most useful tools to understand the physics of earthquake initiation in real faults (Brune, 1979; Abercrombie and Mori, 1996; Malin *et al.*, 2018). Therefore, it is important to improve foreshock observations and characterization, particularly for the more frequent small-to-moderate-size events (i.e., $M_w < 6$), as these might share similar physical processes with larger events. These improved observations may shed light on the physical processes that occur during the triggering and nucleation of earthquakes and will drive future research that focuses on theoretical and numerical models to better characterize earthquake occurrence in real and complex faults.

1. Institut de Sciences de la Terre, Université Grenoble Alpes, CNRS (UMR5275), Grenoble, France; 2. Department of Earth, Atmospheric, and Planetary Sciences, Massachusetts Institute of Technology, Cambridge, Massachusetts, U.S.A.

*Corresponding author: hugo.sanchez-reyes@univ-grenoble-alpes.fr

© Seismological Society of America

Downloaded from http://pubs.geoscienceworld.org/ssa/srl/article-pdf/92/3/1926/5285933/srl-2020253.1.pdf
by IRSN PRP-DGE/Scan/Bertsin user

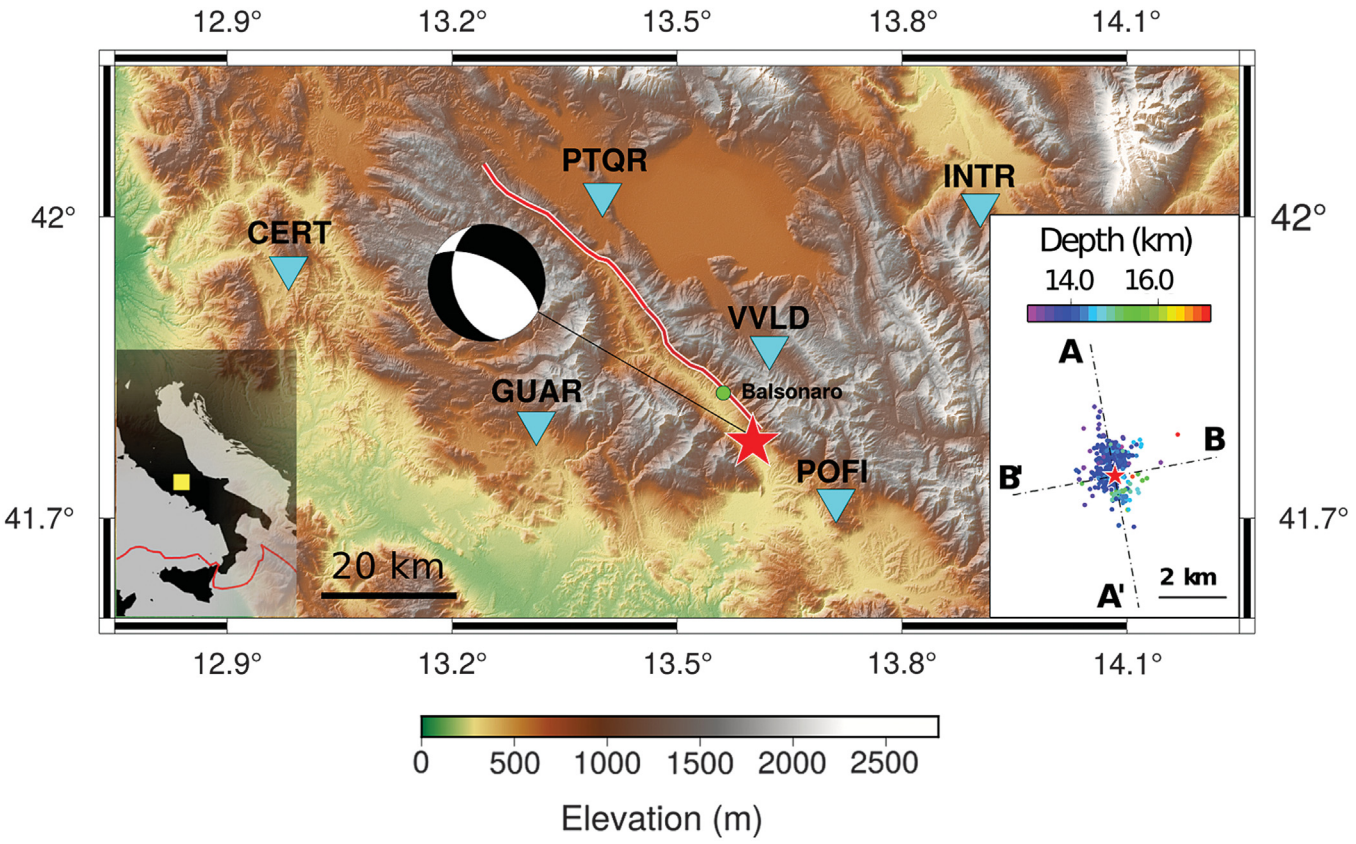

Figure 1. Regional map of the study area. The yellow square inside the small map inset on the left corresponds to the central region of Italy represented in the larger topographic map. The small map inset on the right represents magnification of the area around the epicentral location (red star). The color code used in the map view on the right represents the estimated depth of the foreshock and aftershock activity (estimated in this study: 714 events). The yellow circle represents Balsorano city, and the white triangles represent the stations used in this study. Dashed lines in the right inset map represent the directions A–A′ (along strike) and B–B′ (normal to the strike) illustrated in the cross sections of Figure 5. The solid red line represents the superficial scarp of the Liri fault (scarp taken from Wedmore *et al.*, 2017).

Earthquake initiation (e.g., Kato *et al.*, 2012; Schurr *et al.*, 2014; Tramutoli *et al.*, 2015) and earthquake nucleation (e.g., Dieterich, 1992; Ellsworth and Beroza, 1995; Rubin and Ampuero, 2005) are two different, and perhaps overlapping, phases of the seismic cycle. Although the first is understood to occur over the longer term preceding a large event (i.e., days or months to years), the second occurs some minutes to seconds before the main event. Both phases, however, can be explained under the Dieterich model Dieterich (1994), which relates the seismicity rate to the stressing history through a rate-and-state constitutive law. For earthquake initiation in particular for real faults, two main hypotheses are currently used to explain this process. Some authors argue that a mainshock is a consequence of a cascade process, with stress transfer in between events, which eventually trigger the large event (e.g., Dodge *et al.*, 1996; Ellsworth and Bulut, 2018; Yoon *et al.*, 2019). Alternatively, the initiation of an earthquake can be understood as an aseismic process that weakens the pre-existing asperities, until a larger rupture is promoted (Dodge *et al.*, 1996; Bouchon *et al.*, 2011; Tape *et al.*, 2018). In the latter case, foreshocks result from the activation of brittle asperities by the surrounding aseismic slip processes. However, intermediate models that involve both triggering and aseismic slip are likely for complex faults (e.g., McLaskey, 2019). This complexity might result from fault heterogeneity (e.g., variable stress, frictional properties) and promote imbricated sequences of foreshocks and aseismic slip (e.g., Dublanchet, 2018).

The monitoring of foreshocks is today routine in laboratory experiments (Zang *et al.*, 1998; Goebel *et al.*, 2012; Renard *et al.*, 2019; and references therein), whereas studies that focus on large earthquakes remain relatively sparse (i.e., $M_w > 6$) (e.g., Mogi, 1963; Abercrombie and Mori, 1996; Kato *et al.*, 2012; Bouchon *et al.*, 2013; Chen and Shearer, 2013; Ruiz *et al.*, 2014). However, the recent improvements to seismological monitoring systems around active faults have now provided detailed analysis of foreshocks that precede the more frequent small-to-moderate-size earthquakes ($M_w < 6$) (e.g., McMahon *et al.*, 2017; Savage *et al.*, 2017; Malin *et al.*, 2018). One intriguing feature that has emerged from these more recent studies is the increased complexity (i.e., fault interactions, volumetric processes) that have been revealed through the

Downloaded from http://pubs.geoscienceworld.org/ssa/srl/article-pdf/92/3/1926/5285933/srl-2020253.1.pdf
by IRSN PRP-DGE/Scan/Berssin user

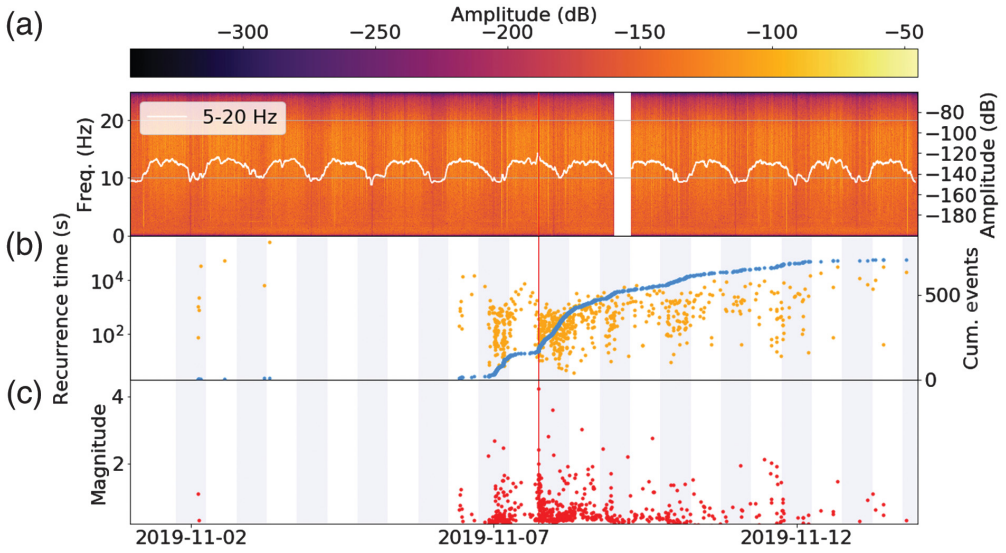

Figure 2. (a) Spectrogram on VVLD.HHZ. The white line is the median of the energy in the frequency band between 5 and 20 Hz calculated within a 1 hr sliding window. Notice the diurnal energy variation. (b) Blue represents cumulative events for the same time period of the experiment and orange represents recurrence time for the newly detected events. (c) Estimated magnitudes for the newly detected events. For illustration purposes, the estimated lowest magnitude shown in (c) is 0. A gap in the continuous data at this receiver location is seen for the night of 8–9 November 2019. In all panels, night periods (18:00–06:00) are represented by shaded regions.

availability of better data (e.g., near-fault receivers) and more advanced detection methods (e.g., template matching) to study foreshocks. This complexity might challenge the actual laboratory scale and theoretical models, which treat earthquake initiation as simple physical processes that occur in smooth fault planes (Dieterich, 1992; Marone, 1998; Liu and Rice, 2005; Rubin and Ampuero, 2005). The necessity for high-resolution characterization of foreshocks based on good data and advanced data processing techniques was also suggested by a meta-analysis carried out by Mignan (2014), which indicated resolution-dependent bias for earthquake initiation models that were resolved using seismological data.

To shed new light on the physical processes that occur before relatively small earthquakes, we study here the medium-sized (M_w 4.4) Balsorano normal fault earthquake and its foreshock–aftershock sequence (Fig. 1). The Italian National Institute of Geophysics and Volcanology (Istituto Nazionale di Geofisica e Vulcanologia [INGV]; online catalog) reported that the main event of this sequence occurred on 7 November 2019 (17:35:21.18 UTC), approximately 4 km southeast of Balsorano city in central Italy (Fig. 1). The hypocenter of this main event was located relatively deep in the crust (14 km), close to the transition zone between the upper and lower crust (10–20 km in depth), where the brittle locked fault transitions into the ductile regime zone (Doglioni *et al.*, 2011). Below this depth, the lower crust is relatively seismically silent (Doglioni *et al.*, 2011). According to a geological study (Roberts and Michetti, 2004), the surface morphology presented by Falcucci *et al.* (2016) and Wedmore *et al.* (2017), together with the main event location and its focal mechanism (Table S1, available in the supplemental material to this article), we assume that this event ruptured a segment of the Liri fault, which is one of the major active normal faults mapped in this region. This structure accommodates the low extension rate observed in this region (i.e., a few millimeters per year) (Westaway, 1992; Hunstad and England, 1999; D'agostino *et al.*, 2001; Roberts and Michetti, 2004). However, we recognize that this assumed geometry (based on the estimated focal mechanism) might be biased, and that the inclusion of body waves into the moment tensor solution (e.g., Zhao and Helmberger, 1994; Zhu and Helmberger, 1996; cut-and-paste method) should improve such estimation.

In addition to the mainshock of 7 November 2019, 135 events occurred close to the epicenter of the main event from 22 October to 15 November 2019 (which included 25 foreshocks). Starting from these cataloged events, we study here the "anatomy" of the foreshocks and aftershocks, and their relationships with the main event. With this aim, continuous data from six three-component stations at less than 75 km from the mainshock epicenter are used (Fig. 1 and Table S2). The continuous waveforms recorded are analyzed using template matching techniques (Gibbons and Ringdal, 2006; Shelly *et al.*, 2007) to detect smaller events and thus to expand upon the available seismic catalog. The detected events are then relocated using the double-difference method (Waldhauser, 2001), to reveal the geometry of the main fault and to obtain new insights into the fault-slip behavior(s) before and after the main seismic event. Furthermore, through waveform clustering, we isolate families of earthquakes that are representative of different physical processes that occur in the pre-mainshock and postmainshock period. This combination of detection, relocation, and waveform clustering reveals an imbricated seismic sequence in which several faults were activated, and with clear differences in the spatiotemporal properties of the foreshocks and aftershocks.

Downloaded from http://pubs.geoscienceworld.org/ssa/srl/article-pdf/92/3/1926/5285933/srl-2020253.1.pdf
by IRSN PRP-DGE/Scan/Bernsin user

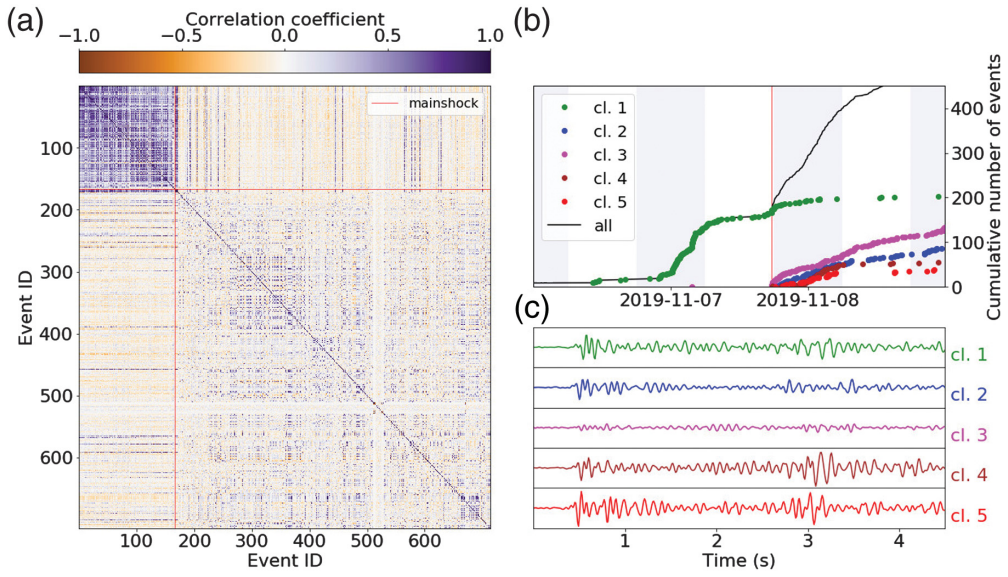

Figure 3. Illustration of the waveform-based hierarchical clustering output. (a) Pairwise correlation coefficients between the waveforms for the vertical component of station VVLD (Fig. 1) of the 714 detected events. This matrix is used to perform the hierarchical clustering. (b) Cumulative events combined with the results from the hierarchical clustering, according to the color code in the legend. (c) Characteristic normalized waveforms (vertical component) of the five different clusters revealed in the earthquake sequence. These traces are obtained after stacking all of the individually normalized waveforms belonging to each cluster.

The final catalog contains 714 events (166 foreshocks and 547 aftershocks), which represents ~six-fold the number of events in the initial catalog. To estimate the magnitudes of the newly detected events, we use the average root mean square in the time window containing the *S* waves over all of the stations and components. Least-square fitting is then used to obtain a linear model that relates the logarithmic of the root mean square of the 23 templates and their local magnitudes from the INGV catalog. This model is then used to estimate the magnitude of the newly detected events. A summary of the event occurrences in time together with their magnitudes is shown in Figure 2.

Methods

Template matching

The analysis starts by extending the INGV seismic catalog using the template matching approach (Gibbons and Ringdal, 2006). From the 135 events reported by the INGV online catalog, in which 25 events are identified as foreshocks, we retain only the events with available *P*- and *S*-wave picks for all of the six stations used. We then extract 4 s of signal, starting 1 s before the phase arrival time from the band-pass filtered data (5–20 Hz). Using the prepicked signals, we estimate the signal-to-noise ratio and retain as templates only those events with a signal-to-noise ratio >3 at all of the stations. With this data selection, 23 events are obtained (including three foreshocks) that are the templates used for scanning the continuous data (Table S4). We use three-component data with *P* waves extracted from the vertical component and *S* waves extracted from the east and north components.

In all, 28 days of continuous data are processed, from 22 October (i.e., 16 days before the mainshock) to 15 November 2019, using the fast matched filter algorithm from Beaucé *et al.* (2017). The detection thresholds are set to 12 times the daily median absolute deviation of the summed correlation coefficients over the array of stations. Finally, consecutive detections with differential times of <3 s are removed (i.e., the time difference between two estimated origin times).

Waveform-based clustering

Clustering is widely used in seismology to recognize patterns in spatiotemporal events, which include the identification of foreshock–aftershock sequences and stress evolution in time (e.g., Kagan and Jackson, 1991; Wehling-Benatelli *et al.*, 2013; Cesca *et al.*, 2014; Ellsworth and Bulut, 2018). Here, we apply a hierarchical clustering analysis (Ward, 1963) to define groups of events inside the earthquake sequence. The dissimilarity between the waveforms of the events in the sequence is used as the distance metric for this clustering analysis. For this analysis, we estimate the dissimilarity (D) between two events, i and j, as $D_{i,j} = 1 - C_{i,j}$ being C_{ij} the correlation coefficient associated with that pair of events. For this, the full normalized waveforms are used to calculate the correlation coefficient, with a 4.5 s time window (starting 0.5 s before the *P*-wave arrival) that contains both the *P* and *S* phase. Under these assumptions, it is important to stress that the events composing a defined group by the hierarchical clustering analysis do not necessarily share similar locations and/or a common rupture mechanism.

The waveforms of the 714 detected events recorded at the closest station to the epicenter (Fig. 1, VVLD) are then correlated with each other. The correlation matrix obtained (Fig. 3a) is used to estimate the distance (dissimilarity) metric to perform hierarchical clustering. The Ward minimum variance method is used (Ward, 1963) with a distance threshold of 5.5 defined (Fig. S1, the largest separation observed from

Downloaded from http://pubs.geoscienceworld.org/ssa/srl/article-pdf/92/3/1926/5285933/srl-2020253.1.pdf
by IRSN PRP-DGE/Scan/Berssin user

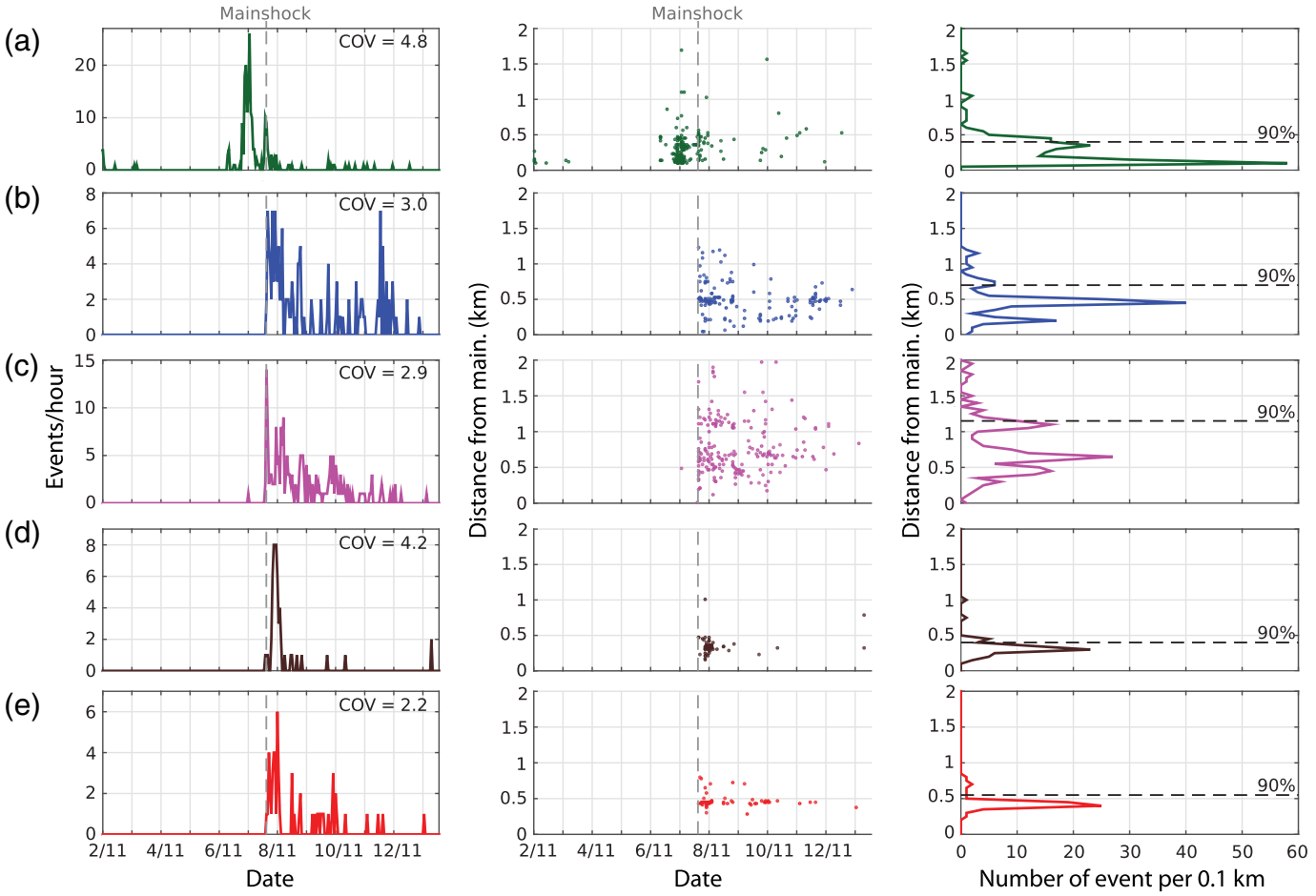

Figure 4. Spatiotemporal evolution of the earthquake sequences with respect to the mainshock origin time and hypocenter. Left panel denotes temporal density (number of events per hour). The coefficients of variation (COV) from the recurrence times are indicated for each cluster. Middle panel denotes distance in time and space from each event of the sequence with respect to the mainshock location and origin time. The dashed gray line on the left and middle panels represents the mainshock origin time. Right panel denotes spatial density (concentration of events per 0.1 km). The dashed black line indicates where 90% of the seismic activity is concentrated. (a–e) Each of the five clusters progressively ordered. The same color code from Figure 3 is used.

the dendrogram). This hierarchical clustering analysis highlights five different groups (clusters), as shown in Figure 3b, c. As both the *P* and *S* waves are used for clustering, the resulting family members might, but not necessarily, share similarities in position and rupture mechanism (Kagan and Jackson, 1991; Cattaneo *et al.*, 1999; Wehling-Benatelli *et al.*, 2013; Cesca *et al.*, 2014; Ellsworth and Bulut, 2018).

Relocation

We finally estimate the relative location between the detected events using the double-difference algorithm (HypoDD software; Waldhauser, 2001). The differential times of the *P* and *S* phases between events from the cross correlation are estimated, with the retention of only the delays that are associated with correlation coefficients >0.6. We further limit the delays to 0.2 s. After discarding the event pairs that relate less than three *P* wave and three *S* wave highly correlated differential times (correlation coefficient ≥0.6), the final number of 29,859 pairs are kept and used in the relocation process.

For each newly detected event, we assume its initial location as the coordinates of the template that reports the highest correlation coefficient related to that event. In addition, we assume the estimated *P*- and *S*-wave picks obtained from our template matching analysis as the initial catalog information for the relocation. A velocity model for this region proposed by Bagh *et al.* (2007) is used in the relocation process (Table S3). Following previous studies (Shelly and Hardebeck, 2019), the inversion is performed with stronger weights to the initial information related to the *P*- and *S*-wave picks from the catalog (i.e., from the template matching analysis), whereas the differential times from the waveform correlations control the final iterations. In the end, 689 of the 714 newly detected events are successfully relocated. The temporal and geometric patterns observed in this earthquake sequence are illustrated in Figures 4 and 5 and are further described in the following section.

Downloaded from http://pubs.geoscienceworld.org/ssa/srl/article-pdf/92/3/1926/5285933/srl-2020253.1.pdf
by IRSN PRP-DGE/Scan/Bertsin user

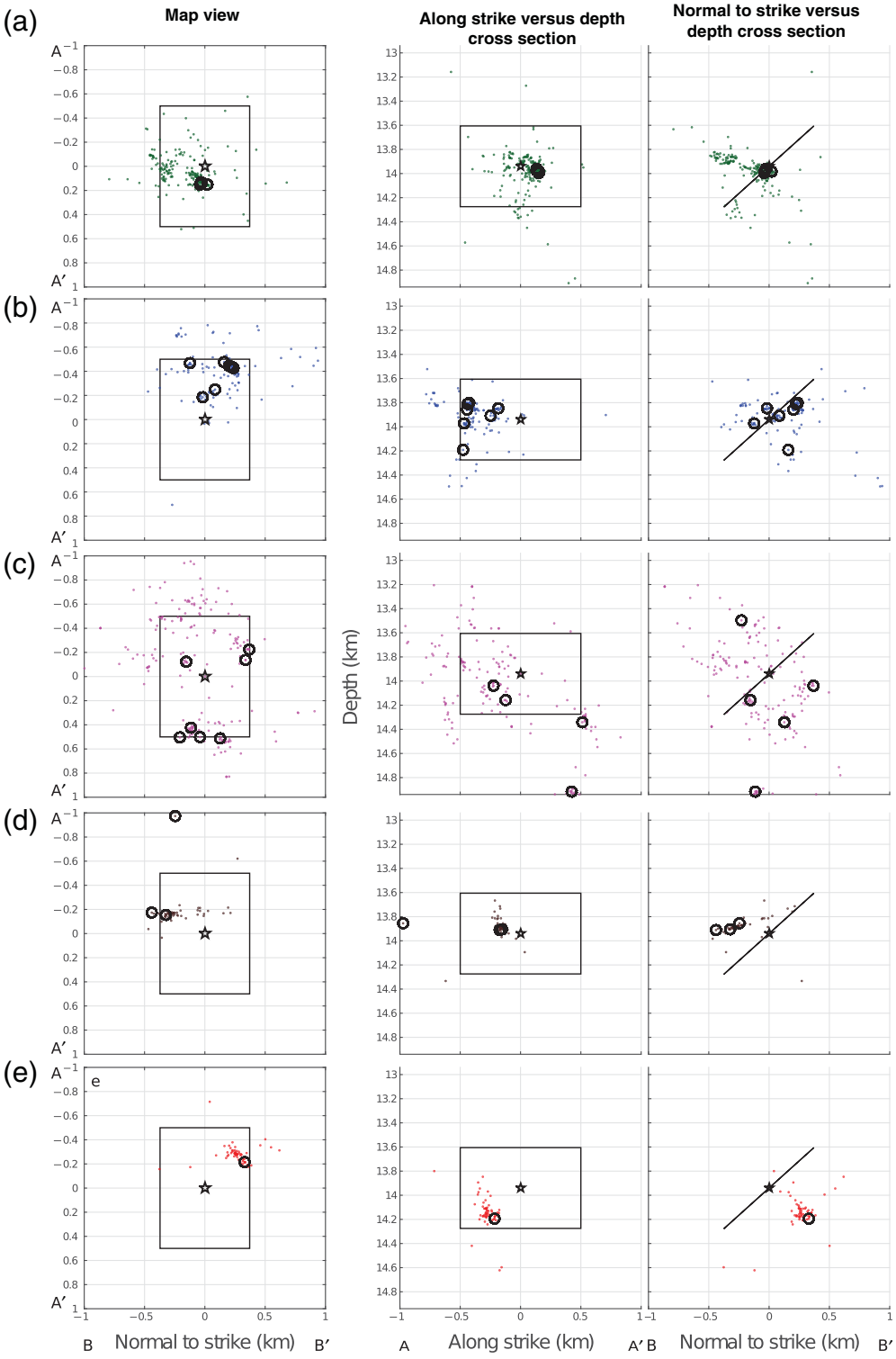

Figure 5. (Left) Map view and (middle) cross sections along the strike, and (right) normal-strike directions for each of the five clusters identified in the sequence (as indicated). All of the locations are relative to the mainshock hypocenter (41.7746° N 13.6066° E; 13.94 km depth, black star). In all of the panels, the same color code is used as in Figures 3 and 4 to represent each different cluster. The solid black line represents a fault plane of 1 km^2 with the geometry of the second nodal plane (Table S1). The directions A–A′ (along strike) and B–B′ (normal to the strike) are the same as in Figure 1. Each cluster is represented by a corresponding label: (a) cluster 1, (b) cluster 2, (c) cluster 3, (d) cluster 4, and (e) cluster 5. In each panel, black circles represent the location of the templates belonging to each cluster.

Results and Discussion

The time evolution of the detected events is shown in Figure 2. Of the 714 events, 166 are foreshocks (23%). Together with the temporal evolution, Figure 2a shows the spectrogram and the average spectral energy in a frequency band from 5 to 20 Hz. The oscillation of this energy suggests variable noise levels in the study area, with lower noise during the night (Fig. 2, shaded areas, for periods from 18:00 to 06:00). This noise variation is related to anthropogenic activity (Poli, Soaga, *et al.*, 2020), and it is also observed for the other five receivers. This noise evolution will probably affect our detection performance. For example, it is not clear if the reduced number of events observed prior to the mainshock is real or is a consequence of the higher noise level (Fig. 2b). We thus avoid discussing any issue related to preseismic quiescence here. However, with the geometric and clustering information derived earlier, we can still characterize some of the properties of the newly detected foreshocks and aftershocks and gain insight into the physical processes that occur at the different stages of the sequence.

The results from the combination of waveform clustering and relocation strategies are summarized in Figures 4 and 5. For each cluster, the coefficient of variation (COV) is also estimated from the recurrence time of the events (Kagan and Jackson, 1991; Schoenball and Ellsworth, 2017). The

Downloaded from http://pubs.geoscienceworld.org/ssa/srl/article-pdf/92/3/1926/5285933/srl-2020253.1.pdf
by IRSN PRP-DGE/Scan/Berssin user

COV indicates the level of the temporal clustering within each group (i.e., how much the occurrence of future earthquakes depends on the occurrence of the past earthquakes): with COV = 1 for random seismicity, and COV > 1 for strong temporal clustering. The larger the COV, the more the earthquakes are interacting. Thus, it is important to note that events that happen together with a high COV mean that there is an intrinsically related interaction between them.

The temporal and spatial densities of the different clusters identified in this sequence are illustrated in Figure 4, in which cluster 1 (green solid lines and dots) is composed mainly of foreshocks (161 of 209 events occurred before the mainshock). The events that form this family show the highest waveform similarity (Fig. 3a). In agreement with this waveform property, cluster 1 has high spatial density, with approximately 90% of its activity (193 of the 208 events) located within 0.5 km of the mainshock hypocenter (Figs. 4a and 5a). Cluster 1 also shows the highest temporal clustering (COV = 4.8; Fig. 4a).

The next two families, as cluster 2 (COV = 3.0; Fig. 4b, blue solid lines and dots) and cluster 3 (COV = 2.9; Fig. 4c, magenta solid lines and dots), share similar temporal clustering values but show differences with respect to their spatial densities. Although approximately 90% of the events of cluster 2 are within 0.8 km of the hypocenter (136 of 151 events; Fig. 4b), cluster 3 has almost 90% of its activity (187 of 211 events) located over a larger volume, as approximately 1.2 km from the mainshock location (Fig. 4c). Cluster 4 (Fig. 4d, brown solid lines and dots) is characterized by 90% of its activity within 0.6 km of the mainshock hypocenter (53 of 59 shocks; Fig. 4d). The seismicity in this cluster is also characterized by high temporal clustering (COV = 4.2). Cluster 5 (COV = 2.2; Fig. 4e, red solid lines and dots) is the least temporally clustered but with the second highest spatial density (after cluster 1), with 90% of its activity in a region 0.5 km from the mainshock hypocenter (66 of 73 events; Fig. 4e). A general spatial pattern of this sequence is the concentration of events close to the mainshock that occurred prior to it (110 foreshocks within 0.3 km) and the subsequent spread over a region >0.3 km during the aftershocks.

Figure 5 illustrates the geometric patterns related to each of the clusters, as defined by the relocation process. A remarkable pattern can be seen in Figure 5a: cluster 1 (i.e., foreshocks) shows an antithetical orientation with respect to the assumed fault plane of the main event (Fig. 5a, map view and cross sections). In contrast, clusters 4 and 5 show nearly parallel orientations with respect to the assumed main fault plane (Fig. 5d,e, cross sections, respectively). We also observe particular behavior for cluster 5, which is the only cluster where the activity is exclusively to the northeast of the mainshock hypocenter and on the footwall (Fig. 5e, map view and cross sections). The events in cluster 5 follow an orientation that is parallel to the assumed main fault plane dipping angle (Fig. 5e, cross section). In turn, cluster 3 has an activity that follows the orientation of the fault plane but that spreads across the whole volume surrounding the fault plane (Fig. 5c, cross sections).

The results of the spatiotemporal evolution for the identified clusters suggest complex evolution of the seismicity. Two fault planes are activated during the sequence, with foreshocks occurring primarily on the antithetic fault plane (Fig. 5a, cross section), similar to part of the foreshock activity that was observed for the L'Aquila normal fault earthquake (Chiaraluce *et al.*, 2011). Relying only on our observations, it is hard to unravel which mechanism(s) might be responsible for the occurrence of the foreshocks, and thus the driving of the main event. For example, there are no exponential or power-law increments of events seen while approaching the main event (Papazachos, 1975; Kagan and Knopoff, 1978), which might suggest accelerating aseismic slip (Dodge *et al.*, 1996; Bouchon *et al.*, 2011; Tape *et al.*, 2018). Neither are any spatial patterns seen (e.g., migrations) that might suggest the same mechanism, or might alternatively indicate triggering by stress transfer (Dodge *et al.*, 1996; Ellsworth and Bulut, 2018; Yoon *et al.*, 2019). However, we clearly outline the differences between the foreshocks and aftershocks. In particular, the foreshocks occur in a more temporal clustered manner, and they are closer to the hypocenter of the main event (Fig. 4a). The compact and highly temporal clustered seismicity indicates strong event interactions and favors stress transfer as the mechanism for foreshock occurrence (COV, Schoenball and Ellsworth, 2017).

To investigate whether aseismic slip triggered, to some extent, the mainshock, we search for seismological evidence such as the existence of repeating earthquakes in the foreshock sequence (Uchida, 2019). The resulting waveform-based correlation matrix (Fig. 3a) shows 118 pairs with correlation coefficients larger than 0.95 (61 pairs of foreshocks and 57 pairs of aftershocks). Regarding the estimated relocation of those highly correlated foreshock waveform pairs, 44 out of the 61 pairs (72%) show a practically overlapping location (relative distances <20 m) considering the uncertainty of the relocation (approximately 20 m). However, the significantly low magnitudes (123 out of 166 foreshocks have magnitudes smaller than 0.5) and the limited frequency range used in our analysis (5–20 Hz) do not allow us to properly reach a conclusion about the existence of repeaters in this sequence (Uchida, 2019; Uchida and Bürgmann, 2019).

Interestingly, the aftershock clusters also show different spatiotemporal behaviors between each other (Figs. 4b–e and 5b–e). The observed differences might be explained by different physical processes driving the aftershock occurrence. For example, clusters 2 and 3 (Fig. 5b,c) spread in a wide volume around the fault in contrast to the other clusters. This spatial pattern is likely to result from stress redistribution, volumetric damage, and relaxation processes after the mainshock (Trugman *et al.*, 2020). In particular, the spatiotemporal evolution of the zone containing cluster 3 expands away from the

Downloaded from http://pubs.geoscienceworld.org/ssa/srl/article-pdf/92/3/1926/5285933/srl-2020253.1.pdf
by IRSN PRP-DGE/Scan/Bernsin user

hypocenter with the logarithm of time (Fig. S6). The spatial expansion of the active zone of cluster 3 is also evidenced by the relatively small amplitude of the stacked waveform estimated for cluster 3 (Fig. 3c). This feature from cluster 3 might suggest afterslip as its driving mechanism (Ross *et al.*, 2017). Such observation might support the alternative model proposed by Inbal *et al.* (2017), in which the afterslip from the mainshock might be the triggering mechanism of the aftershocks off of the main fault. Clusters 4 and 5 in turn are localized in a more compact volume around the assumed fault plane (Fig. 5d,e). This behavior suggests that the activity from these clusters result from a localized stress increment close to the fault plane.

We also search for evidence of repeating earthquakes in the aftershock sequence. Such repeaters may suggest the existence of coplanar afterslip (Nadeau and McEvilly, 1999; Igarashi *et al.*, 2003; Igarashi, 2010). Out of the 57 pairs of highly correlated aftershocks (from the correlation coefficient matrix), 28 show an estimated overlapping location (relative distances <20 m). However, as mentioned earlier, the limited frequency range used and the estimated small magnitudes of the newly detected events do not allow us to conclude whether coplanar afterslip might be the triggering mechanism behind some of these aftershocks.

As in previous studies (McMahon *et al.*, 2017, 2019; Savage *et al.*, 2017), we can see that this detailed analysis of seismic data reveals a complex and imbricated earthquake sequence, for which the mainshock initiation is unlikely to result from only the evolution of physical properties (e.g., stress, friction) on the main fault plane. Indeed the sequence begins through an interaction between the antithetic and main faults during the foreshock–mainshock sequences, similar to that observed for other events (Chiaraluce *et al.*, 2011; McMahon *et al.*, 2019). In normal faults, this behavior can be related to preseismic processes in the dilation wedge located in the hanging wall (Doglioni *et al.*, 2011). The complexity of the sequence might also emerge from fluid involvement, which is known to have a significant role in the control of seismicity and its "style" in the central Apennines (Antonioli *et al.*, 2005; Poli, Marguin, *et al.*, 2020). The stress perturbations in the antithetic fault might have modified the local pore pressures, with fluid migration into the main fault, which would favor the occurrence of the main event (Doglioni *et al.*, 2011).

Conclusion

Using a combination of high-resolution detection methods, precise relocation (e.g., Waldhauser, 2001; Gibbons and Ringdal, 2006), and waveform clustering, we have unveiled the complexity of the sequences associated with the 2019 (M_w 4.4) Balsorano earthquake. We detect 714 events that compose this sequence. These events are classified into five different seismic clusters. The differences between these clusters are highlighted by their distinct spatiotemporal properties that are unveiled by the waveform-based clustering analysis (Kagan and Jackson, 1991; Wehling-Benatelli *et al.*, 2013; Cesca *et al.*, 2014; Ellsworth and Bulut, 2018), and by their relative source locations (Waldhauser, 2001).

Our results highlight different behaviors between foreshocks and aftershocks. For example, foreshocks occur in a compact region near the mainshock hypocenter and show high temporal clustering (Fig. 4a). As mentioned previously, no conclusive evidence of repeating earthquakes in the foreshock sequence could be obtained with the data at hand. In addition, strong temporal clustering and interevent proximity among foreshocks is observed, which might indicate that stress transfer triggering has the main role in driving the occurrence of the foreshocks (Dodge *et al.*, 1996). Nevertheless, there are no observations that can exclude aseismic slip. The foreshock activity takes place mainly in an antithetic fault (Fig. 5a), which suggests that the initiation processes do not only occur on one fault plane but also involve larger volumes (Savage *et al.*, 2017). This precursory antithetic activation has been observed in other normal fault events (Chiaraluce *et al.*, 2011), and it can be expected in some gravity-driven normal fault models (Doglioni *et al.*, 2011).

Furthermore, our analysis shows diversity for the aftershocks' behavior. Indeed, four different clusters compose the aftershock sequences. Cluster 2 is spread in a volume around the main fault (Fig. 5b) and might result from stress redistribution after the mainshock (e.g., caused by volumetric damage and the relaxation processes; Trugman *et al.*, 2020). Cluster 3 exhibits a logarithmic spatial expansion (Fig. S6), which suggests afterslip as its driving mechanism (Ross *et al.*, 2017). According to the rapid temporal decay of their activity, their compactness and spatial orientation, clusters 4 and 5 appear to be driven by rapid stress increments induced by the mainshock and afterslip that occur near the fault plane in the few days after the mainshock (Stein and Lisowski, 1983; Shen *et al.*, 1994).

In summary, this study of foreshocks and aftershocks points out that simple preparation models with evolution of stress and friction on a single fault plane are not suited to precisely explain the evolution of the seismicity we observe here for a real fault. A relatively large volume appears to be involved in the earthquake initiation, over a short time scale (~1 day). We further highlight how the full range of aftershocks is likely to be an ensemble average view of different processes, which will include afterslip, volumetric damage, and relaxation. Continuing to provide detailed information about foreshocks and their relationships to the mainshock and aftershocks also for relatively small events can help us to develop new and more realistic models that can provide better fitting of seismological observations and shed new light on the initiation of earthquakes in real faults.

Data and Resources

The continuous seismic data used in this study are available at the Istituto Nazionale di Geofisica e Vulcanologia (INGV) seismological data center (http://cnt.rm.ingv.it/webservices_and_software/) and were

Downloaded from http://pubs.geoscienceworld.org/ssa/srl/article-pdf/92/3/1926/5285933/srl-2020253.1.pdf
by IRSN PRP-DGE/Scan/Berssin user

downloaded using obspyDMT (https://github.com/kasra-hosseini/obspyDMT, Hosseini and Sigloch, 2017). The fast matched filter (Beaucé *et al.*, 2017) used in this study can be found at https://github.com/beridel/fast_matched_filter. Some plots were made using the Generic Mapping Tools (GMT) version 6.0 and PyGMT (https://www.pygmt.org/latest/index.html; Wessel *et al.*, 2019). The event clustering was performed using Scikit-learn (https://scikit-learn.org/stable/; Pedregosa *et al.*, 2011). Supplemental material for this article includes a PDF file containing five tables and seven figures expanding the information presented in this manuscript as well as MAT file with the whole earthquake catalog obtained from this study. Computations were performed using the University of Grenoble Alpes (UGA) High-Performance Computing infrastructures CIMENT (https://ciment.univ-grenoble-alpes.fr/wiki-pub/index.php/Welcome_to_the_CIMENT_site!). All websites were last accessed in March 2020.

Acknowledgments

This research received funding from the European Research Council (ERC) under the European Union Horizon 2020 Research and Innovation Programme (Grant Agreement 802777-MONIFAULTS). The authors would like to thank the two anonymous reviewers whose comments helped to improve this article. Finally, the authors thank Leoncio Cabrera and the Remote Online Sessions for Emerging Seismologists (ROSES) of the American Geophysical Union Seismology Section, whose help was very useful in the construction of some figures.

References

Abercrombie, R. E., and J. Mori (1996). Occurrence patterns of foreshocks to large earthquakes in the western united states, *Nature* **381,** no. 6580, 303–307.

Antonioli, A., D. Piccinini, L. Chiaraluce, and M. Cocco (2005). Fluid flow and seismicity pattern: Evidence from the 1997 Umbria-Marche (central Italy) seismic sequence, *Geophys. Res. Lett.* **32,** no. 10, doi: 10.1029/2004GL022256.

Bagh, S., L. Chiaraluce, P. De Gori, M. Moretti, A. Govoni, C. Chiarabba, P. Di Bartolomeo, and M. Romanelli (2007). Background seismicity in the central Apennines of Italy: The Abruzzo region case study, *Tectonophysics* **444,** nos. 1/4, 80–92.

Beaucé, E., W. B. Frank, and A. Romanenko (2017). Fast matched filter (fmf): An efficient seismic matched-filter search for both CPU and GPU architectures, *Seismol. Res. Lett.* **89,** no. 1, 165.

Bouchon, M., V. Durand, D. Marsan, H. Karabulut, and J. Schmittbuhl (2013). The long precursory phase of most large interplate earthquakes, *Nature Geosci.* **6,** no. 4, 299–302.

Bouchon, M., H. Karabulut, M. Aktar, S. Özalaybey, J. Schmittbuhl, and M.-P. Bouin (2011). Extended nucleation of the 1999 M_w 7.6 Izmit earthquake, *Science* **331,** no. 6019, 877–880.

Brune, J. N. (1979). Implications of earthquake triggering and rupture propagation for earthquake prediction based on premonitory phenomena, *J. Geophys. Res.* **84,** no. B5, 2195–2198.

Cattaneo, M., P. Augliera, D. Spallarossa, and V. Lanza (1999). A waveform similarity approach to investigate seismicity patterns, *Nat. Hazards* **19,** nos. 2/3, 123–138.

Cesca, S., A. T. Şen, and T. Dahm (2014). Seismicity monitoring by cluster analysis of moment tensors, *Geophys. J. Int.* **196,** no. 3, 1813–1826.

Chen, X., and P. M. Shearer (2013). California foreshock sequences suggest aseismic triggering process, *Geophys. Res. Lett.* **40,** no. 11, 2602–2607.

Chiaraluce, L., L. Valoroso, D. Piccinini, R. Di Stefano, and P. De Gori (2011). The anatomy of the 2009 L'Aquila normal fault system (central Italy) imaged by high resolution foreshock and aftershock locations, *J. Geophys. Res.* **116,** no. B12, doi: 10.1029/2011JB008352.

D'agostino, N., R. Giuliani, M. Mattone, and L. Bonci (2001). Active crustal extension in the central Apennines (Italy) inferred from GPS measurements in the interval 1994–1999, *Geophys. Res. Lett.* **28,** no. 10, 2121–2124.

De Santis, A., D. Marchetti, F. J. Pavón-Carrasco, G. Cianchini, L. Perrone, C. Abbattista, L. Alfonsi, L. Amoruso, S. A. Campuzano, M. Carbone, *et al.* (2019). Precursory worldwide signatures of earthquake occurrences on swarm satellite data, *Sci. Rep.* **9,** no. 1, 1–13.

Dieterich, J. (1994). A constitutive law for rate of earthquake production and its application to earthquake clustering, *J. Geophys. Res.* **99,** no. B2, 2601–2618.

Dieterich, J. H. (1992). Earthquake nucleation on faults with rate-and state-dependent strength, *Tectonophysics* **211,** nos. 1/4, 115–134.

Dodge, D. A., G. C. Beroza, and W. Ellsworth (1996). Detailed observations of California foreshock sequences: Implications for the earthquake initiation process, *J. Geophys. Res.* **101,** no. B10, 22,371–22,392.

Doglioni, C., S. Barba, E. Carminati, and F. Riguzzi (2011). Role of the brittle–ductile transition on fault activation, *Phys. Earth Planet. In.* **184,** nos. 3/4, 160–171.

Dublanchet, P. (2018). The dynamics of earthquake precursors controlled by effective friction, *Geophys. J. Int.* **212,** no. 2, 853–871.

Eftaxias, K., J. Kopanas, N. Bogris, P. Kapiris, G. Antonopoulos, and P. Varotsos (2000). Detection of electromagnetic earthquake precursory signals in Greece, *Proc. Jpn. Acad.* **76,** no. 4, 45–50.

Ellsworth, W. L., and G. C. Beroza (1995). Seismic evidence for an earthquake nucleation phase, *Science* **268,** no. 5212, 851–855.

Ellsworth, W. L., and F. Bulut (2018). Nucleation of the 1999 Izmit earthquake by a triggered cascade of foreshocks, *Nature Geosci.* **11,** no. 7, 531–535.

Falcucci, E., S. Gori, F. Galadini, G. Fubelli, M. Moro, and M. Saroli (2016). Active faults in the epicentral and mesoseismal M_L 6.0 24, 2016 Amatrice earthquake region, central Italy, methodological and seismotectonic issues, *Ann. Geophys.* **59**, doi: 10.4401/ag-7266.

Felzer, K. R., R. E. Abercrombie, and G. Ekstrom (2004). A common origin for aftershocks, foreshocks, and multiplets, *Bull. Seismol. Soc. Am.* **94,** no. 1, 88–98.

Gibbons, S. J., and F. Ringdal (2006). The detection of low magnitude seismic events using array-based waveform correlation, *Geophys. J. Int.* **165,** no. 1, 149–166.

Goebel, T., T. Becker, D. Schorlemmer, S. Stanchits, C. Sammis, E. Rybacki, and G. Dresen (2012). Identifying fault heterogeneity through mapping spatial anomalies in acoustic emission statistics, *J. Geophys. Res.***117,** no. B03310, doi: 10.1029/2011JB008763.

Hosseini, K., and K. Sigloch (2017). Obspydmt: A python toolbox for retrieving and processing large seismological data sets, *Solid Earth* **8,** no. 5, 1047–1070.

Hunstad, I., and P. England (1999). An upper bound on the rate of strain in the central Apennines, Italy, from triangulation

Downloaded from http://pubs.geoscienceworld.org/ssa/srl/article-pdf/92/3/1926/5285933/srl-2020253.1.pdf
by IRSN PRP-DGE/Scan/Bernssin user

measurements between 1869 and 1963, *Earth Planet. Sci. Lett.* **169,** nos. 3/4, 261–267.

Igarashi, T. (2010). Spatial changes of inter-plate coupling inferred from sequences of small repeating earthquakes in Japan, *Geophys. Res. Lett.* **37,** no. 20, doi: 10.1029/2010GL044609.

Igarashi, T., T. Matsuzawa, and A. Hasegawa (2003). Repeating earthquakes and interplate aseismic slip in the northeastern Japan subduction zone, *J. Geophys. Res.* **108,** no. B5, doi: 10.1029/2002JB001920.

Inbal, A., J.-P. Ampuero, and J.-P. Avouac (2017). Locally and remotely triggered aseismic slip on the central San Jacinto fault near Anza, CA, from joint inversion of seismicity and strainmeter data, *J. Geophys. Res.* **122,** no. 4, 3033–3061.

Jones, L. M. (1985). Foreshocks and time-dependent earthquake hazard assessment in southern california, *Bull. Seismol. Soc. Am.* **75,** no. 6, 1669–1679.

Jones, L. M., and P. Molnar (1979). Some characteristics of foreshocks and their possible relationship to earthquake prediction and premonitory slip on faults, *J. Geophys. Res.* **84,** no. B7, 3596–3608.

Kagan, Y., and D. D. Jackson (1991). Long-term earthquake clustering, *Geophys. J. Int.* **104,** no. 1, 117–133.

Kagan, Y., and L. Knopoff (1978). Statistical study of the occurrence of shallow earthquakes, *Geophys. J. Int.* **55,** no. 1, 67–86.

Kato, A., K. Obara, T. Igarashi, H. Tsuruoka, S. Nakagawa, and N. Hirata (2012). Propagation of slow slip leading up to the 2011 Mw 9.0 Tohoku-Oki earthquake, *Science* **335,** no. 6069, 705–708.

Liu, Y., and J. R. Rice (2005). Aseismic slip transients emerge spontaneously in three-dimensional rate and state modeling of subduction earthquake sequences, *J. Geophys. Res.* **110,** no. B8, doi: 10.1029/2004JB003424.

Malin, P. E., M. Bohnhoff, F. Blümle, G. Dresen, P. Martínez-Garzón, M. Nurlu, U. Ceken, F. T. Kadirioglu, R. F. Kartal, T. Kilic, *et al.* (2018). Microearthquakes preceding a M4.2 earthquake offshore Istanbul, *Sci. Rep.* **8,** no. 1, 1–11.

Marone, C. (1998). The effect of loading rate on static friction and the rate of fault healing during the earthquake cycle, *Nature* **391,** no. 6662, 69–72.

McLaskey, G. C. (2019). Earthquake initiation from laboratory observations and implications for foreshocks, *J. Geophys. Res.* **124,** 12,882–12,904.

McMahon, N. D., R. C. Aster, W. L. Yeck, D. E. McNamara, and H. M. Benz (2017). Spatiotemporal evolution of the 2011 Prague, Oklahoma, aftershock sequence revealed using subspace detection and relocation, *Geophys. Res. Lett.* **44,** no. 14, 7149–7158.

McMahon, N. D., W. L. Yeck, M. C. Stickney, R. C. Aster, H. R. Martens, and H. M. Benz (2019). Spatiotemporal analysis of the foreshock–mainshock–aftershock sequence of the 6 july 2017 Mw 5.8 Lincoln, Montana, earthquake, *Seismol. Res. Lett.* **90,** no. 1, 131–139.

Mignan, A. (2014). The debate on the prognostic value of earthquake foreshocks: A meta-analysis, *Sci. Rep.* **4,** 4099.

Mogi, K. (1963). Some discussions on aftershocks, foreshocks and earthquake swarms: The fracture of a semi-infinite body caused by an inner stress origin and its relation to the earthquake phenomena (third paper), *Bull. Earthq. Res. Inst. Univ. Tokyo* **41,** no. 3, 615–658.

Molchanov, O., M. Hayakawa, T. Oudoh, and E. Kawai (1998). Precursory effects in the subionospheric VLF signals for the Kobe earthquake, *Phys. Earth Planet. In.* **105,** nos. 3/4, 239–248.

Nadeau, R. M., and T. V. McEvilly (1999). Fault slip rates at depth from recurrence intervals of repeating microearthquakes, *Science* **285,** no. 5428, 718–721.

Papazachos, B. (1975). Foreshocks and earthquake prediction, *Tectonophysics* **28,** no. 4, 213–226.

Pedregosa, F., G. Varoquaux, A. Gramfort, V. Michel, B. Thirion, O. Grisel, M. Blondel, P. Prettenhofer, R. Weiss, V. Dubourg, *et al.* (2011). Scikit-Learn: Machine learning in Python, *J. Mach. Learn. Res.* **12,**2825–2830.

Poli, P., V. Marguin, Q. Wang, N. D'agostino, and P. Johnson (2020). Seasonal and co-seismic velocity variation in the region of L'Aquila from single station measurements and implications for crustal rheology, *J. Geophys. Res.* **125,** e2019JB019316.

Poli, P., J. Soaga, I. Molinari, V. Cascone, and L. Boschi (2020). The 2020 coronavirus lockdown and seismic monitoring of anthropic activities in northern Italy, *Sci. Rep.* **10,** 1–8.

Reasenberg, P. A. (1999). Foreshock occurrence before large earthquakes, *J. Geophys. Res.* **104,** no. B3, 4755–4768.

Renard, F., J. McBeck, N. Kandula, B. Cordonnier, P. Meakin, and Y. Ben-Zion (2019). Volumetric and shear processes in crystalline rock approaching faulting, *Proc. Natl. Acad. Sci.* **116,** no. 33, 16,234–16,239.

Rikitake, T. (1975). Earthquake precursors, *Bull. Seismol. Soc. Am.* **65,** no. 5, 1133–1162.

Roberts, G. P., and A. M. Michetti (2004). Spatial and temporal variations in growth rates along active normal fault systems: An example from the Lazio–Abruzzo Apennines, central Italy, *J. Struct. Geol.* **26,** no. 2, 339–376.

Ross, Z. E., C. Rollins, E. S. Cochran, E. Hauksson, J.-P. Avouac, and Y. Ben-Zion (2017). Aftershocks driven by afterslip and fluid pressure sweeping through a fault-fracture mesh, *Geophys. Res. Lett.* **44,** no. 16, 8260–8267.

Rubin, A. M., and J.-P. Ampuero (2005). Earthquake nucleation on (aging) rate and state faults, *J. Geophys. Res.* **110,** no. B11, doi: 10.1029/2005JB003686.

Ruiz, S., F. Aden-Antoniow, J. Baez, C. Otarola, B. Potin, F. del Campo, P. Poli, C. Flores, C. Satriano, F. Leyton, *et al.* (2017). Nucleation phase and dynamic inversion of the Mw 6.9 Valparaíso 2017 earthquake in central Chile, *Geophys. Res. Lett.* **44,** no. 20, 210–290.

Ruiz, S., M. Metois, A. Fuenzalida, J. Ruiz, F. Leyton, R. Grandin, C. Vigny, R. Madariaga, and J. Campos (2014). Intense foreshocks and a slow slip event preceded the 2014 Iquique Mw 8.1 earthquake, *Science* **345,** no. 6201, 1165–1169.

Savage, H. M., K. M. Keranen, P. D. Schaff, and C. Dieck (2017). Possible precursory signals in damage zone foreshocks, *Geophys. Res. Lett.* **44,** no. 11, 5411–5417.

Schoenball, M., and W. L. Ellsworth (2017). A systematic assessment of the spatiotemporal evolution of fault activation through induced seismicity in Oklahoma and southern Kansas, *J. Geophys. Res.* **122,** no. 12, 10–189.

Schurr, B., G. Asch, S. Hainzl, J. Bedford, A. Hoechner, M. Palo, R. Wang, M. Moreno, M. Bartsch, Y. Zhang, *et al.* (2014). Gradual

Downloaded from http://pubs.geoscienceworld.org/ssa/srl/article-pdf/92/3/1926/5285933/srl-2020253.1.pdf
by IRSN PRP-DGE/Scan/Berssin user

unlocking of plate boundary controlled initiation of the 2014 Iquique earthquake, *Nature* **512,** no. 7514, 299–302.

Shelly, D. R., G. C. Beroza, and S. Ide (2007). Complex evolution of transient slip derived from precise tremor locations in western Shikoku, Japan, *Geochem. Geophys. Geosyst.* **8,** no. 10, doi: 10.1029/2007GC001640.

Shelly, D. R., and J. L. Hardebeck (2019). Illuminating faulting complexity of the 2017 Yellowstone maple creek earthquake swarm, *Geophys. Res. Lett.* **46,** no. 5, 2544–2552.

Shen, Z.-K., D. D. Jackson, Y. Feng, M. Cline, M. Kim, P. Fang, and Y. Bock (1994). Postseismic deformation following the Landers earthquake, California, 28 June 1992, *Bull. Seismol. Soc. Am.* **84,** no. 3, 780–791.

Singh, R. P., W. Mehdi, R. Gautam, J. Senthil Kumar, J. Zlotnicki, and M. Kafatos (2010). Precursory signals using satellite and ground data associated with the Wenchuan earthquake of 12 May 2008, *Int. J. Rem. Sens.* **31,** no. 13, 3341–3354.

Stein, R. S., and M. Lisowski (1983). The 1979 Homestead Valley earthquake sequence, California: Control of aftershocks and postseismic deformation, *J. Geophys. Res.* **88,** no. B8, 6477–6490.

Tape, C., S. Holtkamp, V. Silwal, J. Hawthorne, Y. Kaneko, J. P. Ampuero, C. Ji, N. Ruppert, K. Smith, and M. E. West (2018). Earthquake nucleation and fault slip complexity in the lower crust of central Alaska, *Nature Geosci.* **11,** no. 7, 536–541.

Tramutoli, V., R. Corrado, C. Filizzola, N. Genzano, M. Lisi, and N. Pergola (2015). From visual comparison to robust satellite techniques: 30 years of thermal infrared satellite data analyses for the study of earthquake preparation phases, *Bol. Geofis. Teor. Appl.* **56,** no. 2, 167–202.

Trugman, D. T., Z. E. Ross, and P. A. Johnson (2020). Imaging stress and faulting complexity through earthquake waveform similarity, *Geophys. Res. Lett.* **47,** no. 1, e2019GL085888, doi: 10.1029/2019GL085888.

Uchida, N. (2019). Detection of repeating earthquakes and their application in characterizing slow fault slip, *Progr. Earth Planet. Sci.* **6,** no. 1, 40.

Uchida, N., and R. Bürgmann (2019). Repeating earthquakes, *Ann. Rev. Earth Planet. Sci.* **47,** 305–332.

Virk, H., and V. Walia (2001). Helium/radon precursory signals of Chamoli earthquake, India, *Radiat. Meas.* **34,** nos. 1/6, 379–384.

Waldhauser, F. (2001). Hypodd-A program to compute double-difference hypocenter locations (hypoDD version 1.0-03/2001), *U.S. Geol. Surv. Open-File Rept. 01*, 113 pp.

Ward, J. H., Jr (1963). Hierarchical grouping to optimize an objective function, *J. Am. Stat. Assoc.* **58,** no. 301, 236–244.

Wedmore, L., J. F. Walker, G. P. Roberts, P. Sammonds, K. McCaffrey, and P. Cowie (2017). A 667 year record of coseismic and interseismic coulomb stress changes in central Italy reveals the role of fault interaction in controlling irregular earthquake recurrence intervals, *J. Geophys. Res.* **122,** no. 7, 5691–5711.

Wehling-Benatelli, S., D. Becker, M. Bischoff, W. Friederich, and T. Meier (2013). Indications for different types of brittle failure due to active coal mining using waveform similarities of induced seismic events, *Solid Earth Discuss.* **4,** no. 2, doi: 10.5194/sed-5-655-2013.

Wessel, P., J. Luis, L. Uieda, R. Scharroo, F. Wobbe, W. Smith, and D. Tian (2019). The generic mapping tools version 6, *Geochem. Geophys. Geosys.* **20,** no. 11, 5556–5564.

Westaway, R. (1992). Seismic moment summation for historical earthquakes in Italy: Tectonic implications, *J. Geophys. Res.* **97,** no. B11, 15,437–15,464.

Yoon, C. E., N. Yoshimitsu, W. L. Ellsworth, and G. C. Beroza (2019). Foreshocks and mainshock nucleation of the 1999 Mw 7.1 Hector Mine, California, earthquake, *J. Geophys. Res.* **124,** no. 2, 1569–1582.

Zang, A., F. Christian Wagner, S. Stanchits, G. Dresen, R. Andresen, and M. A. Haidekker (1998). Source analysis of acoustic emissions in Aue granite cores under symmetric and asymmetric compressive loads, *Geophys. J. Int.* **135,** no. 3, 1113–1130.

Zhao, L.-S., and D. V. Helmberger (1994). Source estimation from broadband regional seismograms, *Bull. Seismol. Soc. Am.* **84,** no. 1, 91–104.

Zhu, L., and D. V. Helmberger (1996). Advancement in source estimation techniques using broadband regional seismograms, *Bull. Seismol. Soc. Am.* **86,** no. 5, 1634–1641.

Manuscript received 23 July 2020
Published online 20 January 2021

Downloaded from http://pubs.geoscienceworld.org/ssa/srl/article-pdf/92/3/1926/5285933/srl-2020253.1.pdf
by IRSN PRP-DGE/Scan/Bernssin user